ACS APPLIED MATERIALS & INTERFACES

www.acsami.org

Research Article

Ball Milling-Enabled $Fe^{2.4+}$ to Fe^{3+} Redox Reaction in Prussian Blue Materials for Long-Life Aqueous Sodium-Ion Batteries

Marcos Lucero, Davis B. Armitage, Xin Yang, Sean K. Sandstrom, Mason Lyons, Ryan C. Davis, George E. Sterbinsky, Namhyung Kim, David M. Reed, Xiulei Ji, Xiaolin Li,* and Zhenxing Feng*

Cite This: *ACS Appl. Mater. Interfaces* 2023, 15, 36366–36372

Read Online

ACCESS | Metrics & More | Article Recommendations | Supporting Information

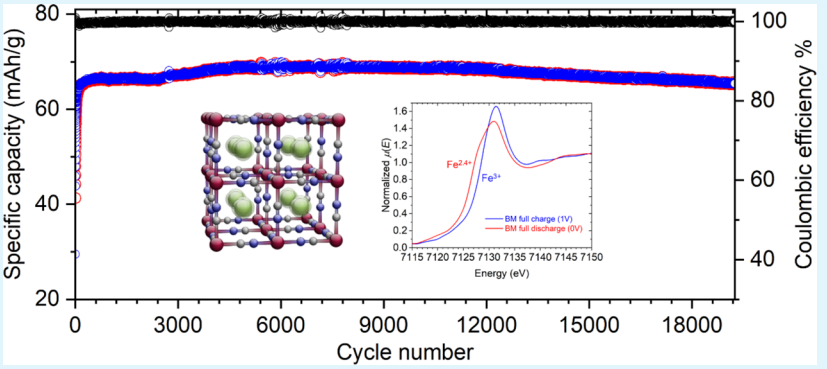

ABSTRACT: Aqueous Na-ion batteries using Prussian blue materials have inherent advantages in safety, material sustainability, and economic cost. However, it is challenging to obtain long-term cycling stability because many redox reactions have poor intrinsic stability in water. Here, we demonstrate reversible $Fe^{2.4+}$ to Fe^{3+} redox reaction of Prussian blue electrodes cycled in a 17 m $NaClO_4$ water-in-salt electrolyte. The cubic phase c-$Na_{1.17}Fe[Fe(CN)_6]\cdot 0.35H_2O$) derived from monoclinic Prussian blue (m-$Na_{1.88}Fe[Fe(CN)_6]\cdot 0.7H_2O$) through ball milling delivers excellent cycling stability of >18,000 cycles with >90% capacity retention at the 10C rate. The specific capacity is ∼75 and ∼67 mAh/g at 1C and 10C rates, respectively. Systematic characterizations including electron microscopy, X-ray diffraction, Fourier-transform infrared spectroscopy, X-ray photoelectron spectroscopy, and X-ray absorption spectroscopy have verified the phase transition and iron oxidation state evolution, revealing the mechanism that enables the material's high rate and long durability as the battery cathode.

KEYWORDS: *aqueous sodium-ion batteries, Prussian blue analogues, water-in-salt, ball milling, electrolytes, X-ray absorption spectroscopy*

INTRODUCTION

Rechargeable batteries are crucial for harnessing renewable energy from solar and wind and releasing them in times of need. To expedite the energy transition to renewable and sustainable energy resources, highly efficient batteries composed of earth-abundant elements are needed. Currently, the lithium-ion battery (LIB) is leading the charge in the renewable energy transition and is deployed in much-needed applications including electric vehicles (EV), and large-scale stationary energy storage (SES). However, the safety concern and the localized deposits of lithium on the earth can cause high cost and supply issues, which motivates research in alternative battery chemistries. One area where next-generation rechargeable batteries can alleviate the need for LIBs is in large-scale SES applications. The aqueous sodium-ion battery (ASIB) is a promising candidate over conventional LIBs with nonaqueous electrolyte or aqueous LIBs.[1] The major advantages of ASIBs are the ubiquitous distribution of sodium in earth's crust and oceans and the low cost and high safety (e.g., nonflammable) of the aqueous electrolytes.

The ASIB technology requires electrode materials with excellent electrochemical performance and sustainability. A promising class of materials is the Prussian blue analogues (PBAs) with the chemical formula $Na_{2-x}M_a[M_b(CN)_6]\cdot zH_2O$ ($M_{a,b}$ = Fe, Mn, Ni, etc.). The PBA consists of a framework structure where cyano $(C\equiv N)^-$ anions link transition metal ions in a three-dimensional array.[2] These materials have several advantages over other intercalation compounds including a straightforward low-temperature synthesis, reversible extraction of maximum of two Na ions per chemical formula, and

Received: May 22, 2023
Accepted: July 7, 2023
Published: July 23, 2023

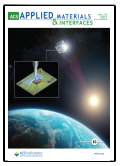

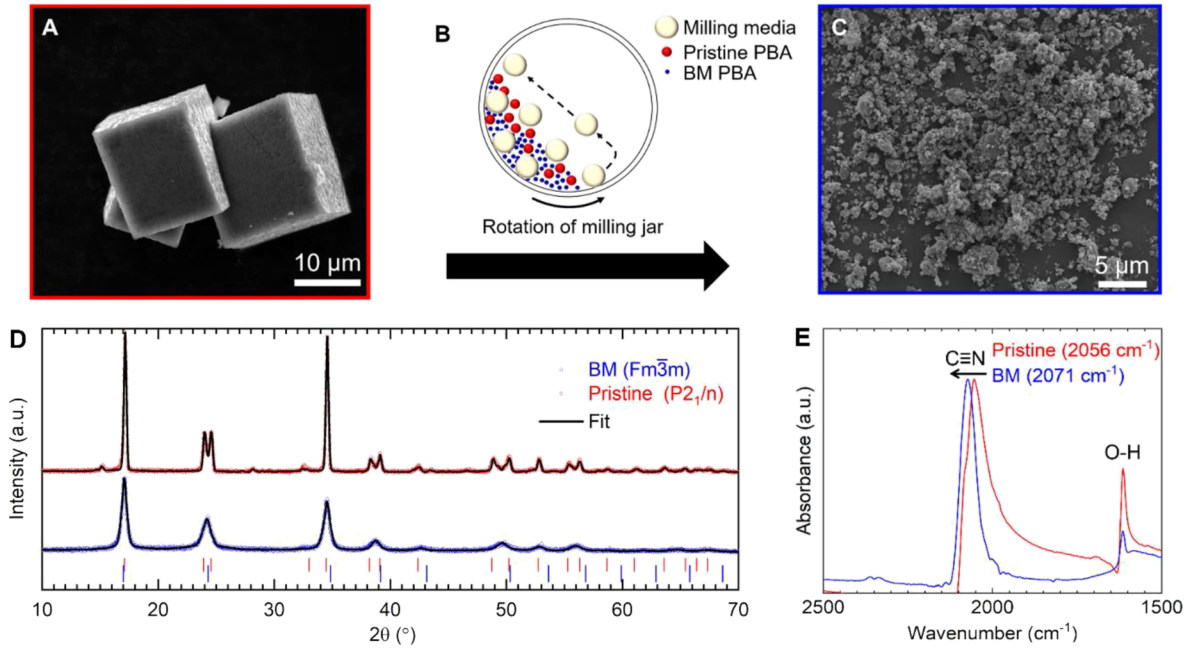

Figure 1. Structural characterization of PBA materials. (A) Typical SEM image of the pristine PBA (monoclinic $P2_1/n$). (B) Schematic of the ball milling modification process. (C) SEM image of ball-milled PBA (cubic $Fm\bar{3}m$). (D) Powder XRD and Rietveld refinement. (E) FT-IR spectra of pristine and ball-milled PBA.

large crystalline channels for the highly reversible insertion/extraction at low and high C rates. These materials can incorporate Li^+, Na^+, K^+, NH_4^+, Ca^{2+}, and Mg^{2+} into the structure, making them suitable electrodes for diverse battery chemistries.[3−5] Multiple research groups have shown the use of PBA such as $Na_2MnFe(CN)_6$ and $Na_2CuFe(CN)_6$ for SIB and have demonstrated promising electrochemical performance.[1,6] However, the incorporation of numerous transition metals will increase the difficulty of the synthesis and cost based on the specific transition metals precursors.[5,6] Exclusive incorporation of abundant and low-cost Fe would yield a low-cost and sustainable electrode material.[7,8] Furthermore, several groups have demonstrated that iron-based PBA, sodium hexacyanoferrate, ($Na_2Fe[Fe(CN)_6]$), can have excellent electrochemical performance with highly reversible extraction/insertion of ∼2 Na ions with a high capacity of ∼170 mAh/g, making it a highly promising cathode material for ASIB.[7,8]

However, Fe-based redox has an intrinsic instability in aqueous electrolytes. It has been well acknowledged that the O_2 dissolved in the H_2O can limit the capacity and cycling stability delivered by electrode materials. Specifically, O_2 can chemically oxidize the reduced state of the electrode material, thereby interfering with the electrochemical reaction.[9,10] However, methods can be developed to reduce this effect.[9,11,12] One common method is through surface coatings, Luo et al., demonstrated that carbon-coated $LiFePO_4$ has been shown to significantly improve the chemical stability of the redox couple in aqueous electrolyte.[11]

In this work, we achieved the $Fe^{2.4+}/Fe^{3+}$ redox reaction in PB material by converting the monoclinic sodium iron hexacyanoferrate (m-$Na_{1.88}Fe[Fe(CN)_6]\cdot 0.7H_2O$) to cubic phase (c-$Na_{1.17}Fe[Fe(CN)_6]\cdot 0.35H_2O$) through the ball milling modification process and demonstrated high cycling performance in a 17 m $NaClO_4$ water-in-salt electrolyte. The $Na_{1.17}Fe[Fe(CN)_6]\cdot 0.35H_2O$ was obtained by ball milling the pristine $Na_{1.88}Fe[Fe(CN)_6]\cdot 0.7H_2O$, (PBA) with carbon additive Ketjen black. The ball milling introduced a unique phase transition from monoclinic to cubic, confirmed by systematic characterization including electron microscopy, X-ray diffraction (XRD), Fourier-transform infrared spectroscopy (FT-IR), and X-ray photoelectron spectroscopy (XPS). X-ray absorption spectroscopy (XAS) verified the iron oxidation state evolution in the redox reaction. The cubic phase $Na_{1.17}Fe[Fe(CN)_6]\cdot 0.35H_2O$ delivers a specific capacity of ∼75 and ∼67 mAh/g at 1C and 10C rates, respectively. Excellent cycling stability with >90% capacity retention over >18,000 cycles was obtained. The significant increase in the performance of the cubic PBA compound makes it a suitable high-performance cathode for ASIB.

RESULTS AND DISCUSSION

Cubic Phase $Na_{1.17}Fe[Fe(CN)_6]\cdot 0.35H_2O$. The as-received PBA material $Na_{1.88}Fe[Fe(CN)_6]\cdot 0.7H_2O$, hereafter referred to as pristine PBA, has a cuboidal morphology with clusters of intergrown cubes.[2,7,8] As shown in the scanning electron microscopy (SEM) images in Figure 1A, the cubic structures have dimensions in the range of tens of micrometers and exhibit a uniform elemental distribution (Figure S1). After a simple ball milling process (Figure 1B) in the presence of a conductive carbon additive, the large primary particles and agglomerates lose the cubic morphology and became small particles with random morphologies and sizes ranging from hundreds of nanometers to a few micrometers (Figure 1C). The conductive carbon was utilized to increase the electrical conductivity of the PBA material to promote more facile Na-ion insertion/extraction,[13] while serendipity has led to a unique phase transition and Fe oxidation state change of the ball-milled PBA (denoted as BM PBA).

Powder XRD (Figure 1D) clearly shows different patterns for the pristine and BM PBA samples. Doublet peaks at 2θ values of ∼25, ∼38, ∼50, and ∼55° turned into singlet peaks after ball milling.[7,14] Rietveld refinement of the powder XRD

https://doi.org/10.1021/acsami.3c07304
ACS Appl. Mater. Interfaces 2023, 15, 36366−36372

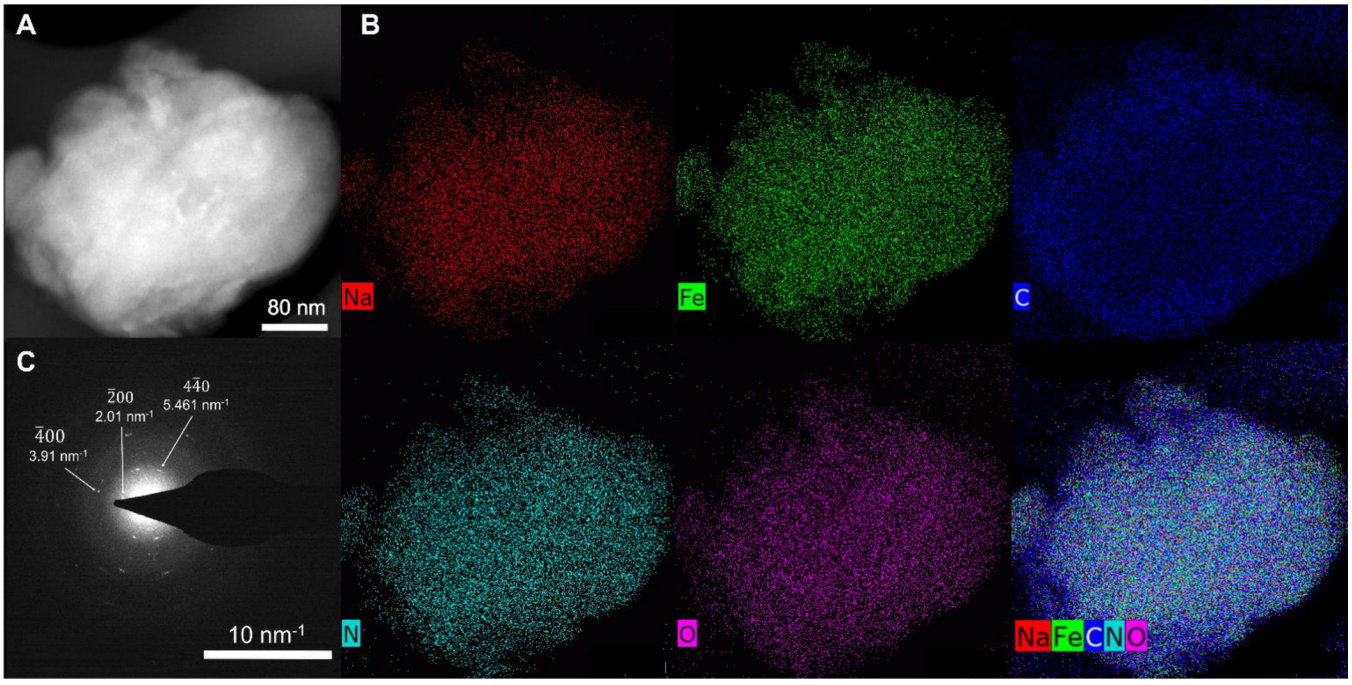

Figure 2. Morphology and structure analysis of ball-milled PBA. (A) Representative STEM image of a ball-milled PBA particle. (B) Elemental mapping of the particle. (C) Selected area electron diffraction (SAED) pattern of the particle.

data for the pristine PBA revealed a monoclinic $P2_1/n$ space group with a composition of $Na_{1.88}Fe[Fe(CN)_6]\cdot 0.7H_2O$ and excellent crystallinity (See Figure S2).[7,15] The lattice parameters are a = 10.4452 Å, b = 7.4443 Å, c = 7.4651 Å, α = 90°, β = 92.1673°, γ = 90° (R_{wp} = 8.60%) (See Table S1). Analysis of BM PBA by powder XRD revealed a composition of $Na_{1.17}Fe[Fe(CN)_6]\cdot 0.35H_2O$ and a phase transition to cubic $Fm\bar{3}m$ indicated by the decreased intensity and peak broadening (See Figure S3). The broadening effect is known to occur for powders with small particle sizes, but it is also observed for sodium-deficient or sodium-free cubic PBA phases (e.g., PB or Berlin green).[2,4,14,16] Rietveld analysis on BM PBA was performed using two different space groups, monoclinic $P2_1/n$, and cubic $Fm\bar{3}m$, to confirm the phase transitioning of BM PBA by the ball milling process. Model-based fitting of BM PBA utilizing a monoclinic $P2_1/n$ structure yielded unsatisfactory convergence (R_{wp} = 15.77%) (Figure S4), while the cubic space group $Fm\bar{3}m$ provided far more satisfactory fit (R_{wp} = 4.22%). Rietveld refinement parameters for BM PBA reveal lattice parameters $a = b = c$ = 10.33291 Å, and $\alpha = \beta = \gamma$ = 90° (Tables S2 and S3). The changes observed for the BM PBA indicate that the ball milling process decreases the sodium content in the material which we believe causes the phase change.[4,16] This finding is supported by the literature, and it has been observed that desodiation of PBA is known to cause rhombohedral to cubic phase change.[17]

Fourier-transform infrared spectroscopy (FT-IR) is a common technique that has been previously used to study PBA materials as changes in the sodium content of PBA result in varying cyano stretching (ν(C≡N)) modes.[18] In Figure 3E, the cyano stretch (ν(C≡N)) values are 2056 and 2071 cm^{-1} for pristine and BM PBA, respectively.[2,18] This blue shift is commonly observed when transitioning from a fully filled PB (or Prussian white) framework (i.e., monoclinic) to a partially filled PB framework in agreement with powder XRD.[2,18−20]

Besides the crystalline structure and vibrational stretching modes in the PBA framework, changes in sodium content also affect the oxidation state of Fe in the PBA framework. In the fully filled framework (e.g., $Na_2Fe[Fe(CN)_6]$), the oxidation state of Fe is 2+, while in the half-filled structure (e.g., $Na_1Fe[Fe(CN)_6]$) and empty structure (e.g., $Fe[Fe(CN)_6]$), the average oxidation state of Fe is 2.5+ and 3+, respectively.[2,21] Utilizing XPS, we observed the changes in oxidation state for the pristine and BM PBA. In Figure S5, we observe noticeable changes in the Fe 2p narrow scan, while the pristine PBA shows the characteristic Fe^{2+} satellite features adjacent to the Fe $2p_{3/2}$ and Fe $2p_{1/2}$ peaks. These satellite features shift away from the main photoexcitation line to higher binding energies for the BM PBA indicating that the Fe in the framework has been oxidized.[21,22]

Scanning transmission electron microscopy (STEM) measurements were carried out to further characterize the BM PBA material. STEM images in Figure 2A show the typical small particle with a size in the hundred-nanometer range. The chemical composition of the material was measured using energy dispersive spectroscopy (EDS). The elemental mapping in Figure 2B reveals a homogeneous distribution of Na, Fe, C, N, and O. Quantitative analysis (Figure S6) of the elemental composition reveals a Na and Fe composition of 38.44% Na and 61.56%, respectively. It confirms our hypothesis that ball milling lowers the sodium content in the framework and is in good agreement with the sodium content of 1.17 Na per chemical formula ($Na_{1.17}Fe[Fe(CN)_6]\cdot 0.35H_2O$). Selected area electron diffraction (SAED) of the BM PBA in Figure 2C can be indexed to the cubic $Fm\bar{3}m$ space group, in agreement with Rietveld refinement in Figure 1D.[23] The $\bar{2}00$, $\bar{4}00$, $4\bar{4}0$ have values of 2.01, 3.91, and 5.46 nm^{-1}, respectively, and match the theoretical values for cubic PBA.

Electrochemical Performance. The electrochemical performance of the PBA materials was examined by cyclic voltammetry (CV) and galvanostatic charge−discharge meas-

https://doi.org/10.1021/acsami.3c07304
ACS Appl. Mater. Interfaces 2023, 15, 36366−36372

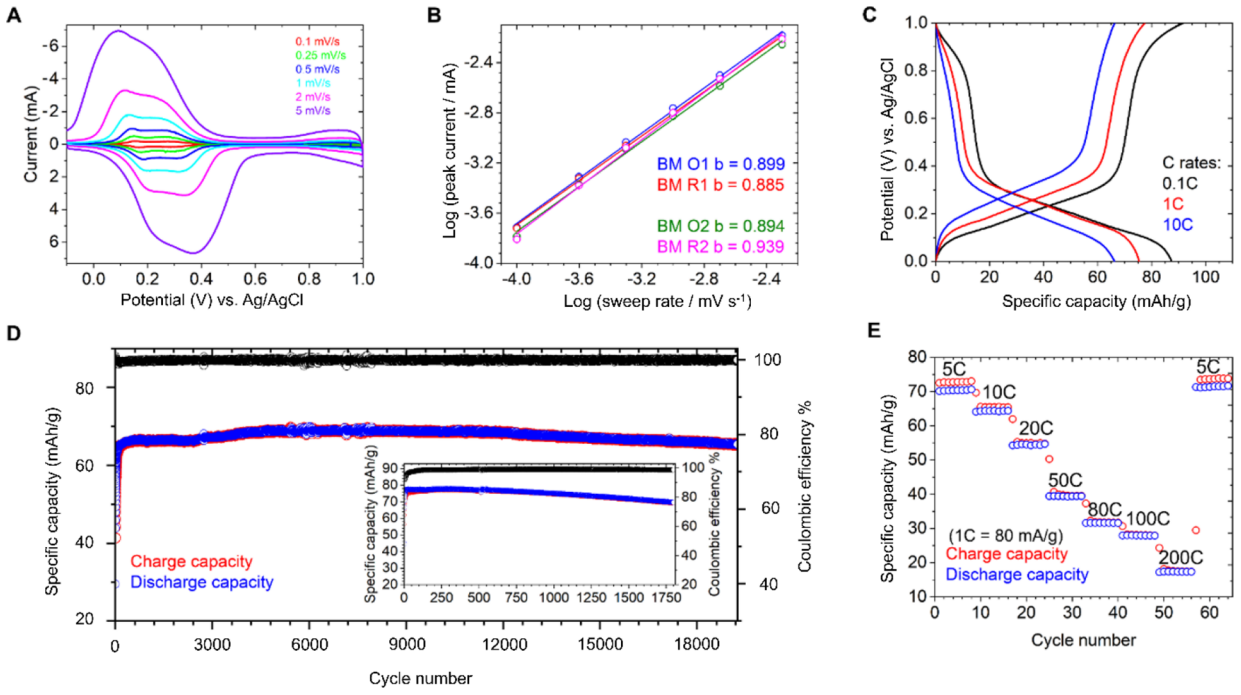

Figure 3. Electrochemical characterization of the PBA electrodes. (A) CV curves measured at different scan rates. (B) The analysis of the peak current and the scan rate. (C) GCD curves at different rates. (D) Long-term cycling for ball-milled PBA at 10C (inset 1C charging). (E) Rate capability test from 5C to 200C.

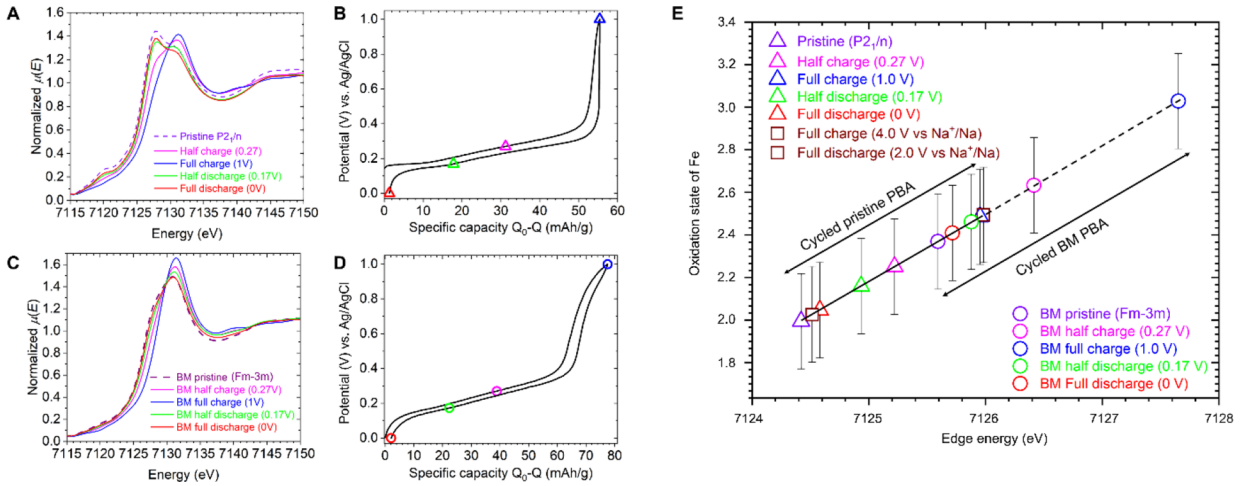

Figure 4. Investigation of Na-insertion mechanism in PBA before and after ball milling. (A) XANES at Fe K-edge for as-received PBA at different SOCs. (B) GCD curve showing the different SOCs for as-received PBA. (C) XANES at Fe K-edge for ball-milled PBA at different SOC. (D) GCD curve showing the different SOCs for BM PBA. (E) Oxidation state analysis based on centroid of the Fe K-edge (e.g., Edge energy).

urements. Electrochemical data for pristine PBA can be found in Figure S7−S10. Figure 3A shows the CV of BM PBA. At a scan rate of 0.1 mV s^{-1}, the set of iron redox peaks appears at 0.17/0.16 V (O1/R1) and 0.29/0.27 V (O2/R2), which are similar to those found in $LiFePO_4$, 0.16/0.36 (O/R).[24,25] The electrochemical characteristics of our electrodes were investigated by increasing the scan rates from 0.1 to 5 mV s^{-1}. The following equation $i = av^b$ was utilized to study electrode kinetics, b values of 0.9/0.89 and 0.89/0.93 were found for the two sets of oxidation/reduction peaks as seen in Figure 3B.[4,26−28] This intercalation pseudocapacitative response is due to the small dimension and high surface area of the primary particles.[29,30] These two factors promote a facile Na-ion insertion/extraction mechanism and amplify the pseudocapacitive character of the battery electrode.[29,30] The Faradaic nature of this mechanism will be explored and supported by bulk-sensitive XAS.

Galvanostatic charge−discharge (GCD) measurements were performed within the potential window of 0−1 V vs sat. Ag/AgCl and were first charged followed by discharging to complete a full cycle (Figure 3C). Long-term cycling in Figure 3D reveals low capacities of 40 and 45 mAh/g for 10C and 1C in the initial cycles, respectively. However, the charge−discharge capacities begin to increase after ∼40 h and reach a stable maximum value of ∼75 and ∼65 mAh/g for cycling rates of 1C and 10C, respectively. We attribute the truncated capacity values in the initial cycle to insufficient wetting of the electrode caused by the hydrophobic behavior of the PVDF

https://doi.org/10.1021/acsami.3c07304
ACS Appl. Mater. Interfaces 2023, 15, 36366−36372

binder to the water-in-salt electrolyte. Switching to a hydrophilic binder could improve the wetting of the electrode, which will be used in our future experiments. Within ~40 h, the electrode becomes sufficiently wetted and give rise to stable electrochemical cycling. The BM PBA delivers a reversible capacity of 87, 75, and 65 mAh/g at C rates of 0.1C, 1C, and 10C (1C = 80 mAh/g) after formation cycles as shown in Figure 3C. At the different C rates, the charge−discharge curve displays similar features with plateaus centered on 0.27 and 0.17 V vs Ag/AgCl for charge and discharge, respectively. Furthermore, the cells demonstrate a capacity retention of 96% after 1750 and 18,000 cycles for 1C and 10C, respectively (Figure 3D). Aside from good stability, the BM PBA exhibits fine capacity utilization in the high-rate capability test. In Figure 1E, the discharge capacity is 70, 65, 55, 40, 35, 30, and 18 mAh/g at 5C, 10C, 20C, 50C, 80C, 100C, and 200C rates. This is a significant increase in capacity over the pristine PBA which only delivers a capacity of ~35 mAh/g at 10C.

$Fe^{2.4+}$ to Fe^{3+} Redox Reaction. To understand the fundamental reason for the high stability, the redox reaction mechanism upon Na-insertion/desertion was investigated through X-ray absorption fine edge structure (XANES) at the Fe K-edge which provides oxidation state and local structure information.[31−34] It is natural that the Na-ion insertion/extraction will result in the oxidation state of Fe in the PBA framework to change.[26,31,35] In the fully filled framework, Prussian white ($Na_2Fe[Fe(CN)_6]$), the theoretical oxidation state of Fe is 2+. When Na-ions are extracted the oxidation state of Fe increases, in the case of a half-filled ($NaFe[Fe(CN)_6]$) and empty ($Fe[Fe(CN)_6]$) framework, the average oxidation states of Fe are 2.5+ and 3+, respectively. The Fe oxidation states in the practical charge−discharge process can be outlined by measuring the Fe K-edge XANES of the pristine PBA and BM PBA at different states of charge and subsequently the sodium content in the structures.[34,36]

Figure 4B,D shows the GCD curves for the PBA materials and the states of charge for potentials at which XANES measurements were taken. Cell potentials of 0.25 V (half charge) and 1 V (full charge) vs Ag/AgCl and discharged to 0.17 V (half discharge) and 0 V (full discharge) vs Ag/AgCl were chosen based on electrochemical measurements in Figure 3. During charge, Na-ions are removed from the structure and Fe in the framework becomes oxidized. The opposite occurs during discharge, where Na-ions are inserted into the framework and Fe in the framework is reduced. The Fe K-edge XANES reveals the redox reaction during cycling.[37,38] In pristine PBA, the Fe K-edge shifts to higher energies when charged from the pristine state to the fully charged state from 7124.4 to 7126 eV (oxidation) and shifts back to lower energies when fully discharged to 7124.6 eV (reduction) (Figure 4A,E). Using the integral method, the Fe K-edge was utilized to determine edge shifts in the XANES.[31,33,34,39] The oxidation state of the pristine PBA was assigned to 2+, while fully charged pristine PBA cycled to 4.0 V vs Na^+/Na in organic electrolytes was assigned to 2.5+. A linear fit between pristine and fully charged PBA standards was utilized to determine intermediate oxidation state values and oxidation states beyond this region were extrapolated.

The BM PBA exhibits a similar trend but in a different range. When charged from the pristine to the fully charged state, Fe K-edge shifts from 7125.5 and 7127.8 eV, and when fully discharged the edge shifts back to 7125.7 eV. The higher edge position at OCV (7125.6 eV) of the BM PBA indicates a greater oxidation state of 2.4+ to start with, corroborating the results in Figure 1 on Na-ion deficiency and Fe oxidation. At the fully charged state, the oxidation state of Fe for BM PBA is 3+ .

Aside from edge shifts, noticeable changes in the pre-edge feature are observed for the PBA materials. These pre-edge features can give insight into the local structure of the probed element (e.g., Fe).[40] Upon charging, the intensity of the pre-edge feature in the XANES for the pristine PBA decreases and disappears at the fully charged state. This decreased intensity is a sign that the local structure around Fe has become more symmetric after Na-ion extraction. For the case of BM PBA, the pre-edge feature is almost absent. This suggests that Na-ion extraction leads to a phase transition from monoclinic to cubic given the similarity in line shape and edge position of pristine and BM PBA and agreement with previous studies.[36,38,40]

Electrochemical data reveal an increase in capacity for BM PBA and we attribute this increase to morphology and crystal structure changes. The BM PBA is able to deliver a great capacity of 75 mAh/g compared to 50 mAh/g for the pristine PBA at a rate of 1C. The particle size of BM PBA is significantly reduced making the Na-insertion/extraction mechanism more facile due to the larger surface area available and shorter diffusion length for Na-ions. The greater amount of Na-ion utilization is captured by XANES. As seen in Figure 4E, BM PBA exhibits a wider window of oxidation as indicated by the larger shift in the edge position compared to the pristine PBA and supports the faradaic nature of the electrochemical reaction. Based on the edge position, it was determined that Pristine PBA operates between ($Fe^{2+}/Fe^{2.5+}$), while BM operates between ($Fe^{2.4+}/Fe^{3+}$). In addition, the long-term stability of BM PBA enabled by the ball milling processing can be attributed to the slight structure changes of the cubic $Na_{1.17}Fe[Fe(CN)_6]\cdot 0.35H_2O$ upon charging and discharging, as revealed by EXAFS, which is similar to what we found before in $Na_3Fe_3(PO_4)_4$ as anode for ASIB application.[26]

CONCLUSIONS

In this work, we induced the monoclinic sodium iron hexacyanoferrate (m-$Na_{1.88}Fe[Fe(CN)_6]\cdot 0.7H_2O$) to a cubic phase (c- $Na_{1.17}Fe[Fe(CN)_6]\cdot 0.35H_2O$) transition by simple ball milling of the PB material. By serendipity, the sodium deficiency and unique phase transition caused by ball milling enables highly reversible $Fe^{2.4+}$ to Fe^{3+} redox reaction of the PB material in the water-in-salt electrolyte. The aqueous SIB using the BM PBA delivers a high specific capacity and excellent cycling stability and rate performance. Our discovery that Na content change in PBA can control phase transition and tune the Fe oxidation states, not only developed an advanced PBA material but also provides insight into the future design of PBA materials for battery applications.

ASSOCIATED CONTENT

Supporting Information

The Supporting Information is available free of charge at https://pubs.acs.org/doi/10.1021/acsami.3c07304.

Experimental methods, Rietveld refinement tables, physical characterization information (e.g., EDS, XRD, XPS, STEM-EDS and EXAFS), and electrochemical data (e.g., GCD and CV) (PDF)

https://doi.org/10.1021/acsami.3c07304
ACS Appl. Mater. Interfaces 2023, 15, 36366−36372

AUTHOR INFORMATION

Corresponding Authors

Xiaolin Li − *Pacific Northwest National Laboratory, Richland, Washington 99352, United States;* orcid.org/0000-0002-7728-0157; Email: xiaolin.li@pnnl.gov

Zhenxing Feng − *School of Chemical, Biological, and Environmental Engineering, Oregon State University, Corvallis, Oregon 97331, United States;* orcid.org/0000-0001-7598-5076; Email: zhenxing.feng@oregonstate.edu

Authors

Marcos Lucero − *School of Chemical, Biological, and Environmental Engineering, Oregon State University, Corvallis, Oregon 97331, United States; Pacific Northwest National Laboratory, Richland, Washington 99352, United States*

Davis B. Armitage − *School of Chemical, Biological, and Environmental Engineering, Oregon State University, Corvallis, Oregon 97331, United States*

Xin Yang − *Pacific Northwest National Laboratory, Richland, Washington 99352, United States*

Sean K. Sandstrom − *Department of Chemistry, Oregon State University, Corvallis, Oregon 97331, United States*

Mason Lyons − *School of Chemical, Biological, and Environmental Engineering, Oregon State University, Corvallis, Oregon 97331, United States;* orcid.org/0000-0001-8729-3376

Ryan C. Davis − *Stanford Synchrotron Radiation Lightsource, SLAC National Accelerator Laboratory, Menlo Park, California 94025, United States*

George E. Sterbinsky − *X-ray Science Division, Argonne National Laboratory, Lemont, Illinois 60439, United States;* orcid.org/0000-0002-1451-5035

Namhyung Kim − *Pacific Northwest National Laboratory, Richland, Washington 99352, United States*

David M. Reed − *Pacific Northwest National Laboratory, Richland, Washington 99352, United States*

Xiulei Ji − *Department of Chemistry, Oregon State University, Corvallis, Oregon 97331, United States;* orcid.org/0000-0002-4649-9594

Complete contact information is available at: https://pubs.acs.org/10.1021/acsami.3c07304

Notes

The authors declare no competing financial interest.

ACKNOWLEDGMENTS

This work is supported by the National Science Foundation under grant no. CBET-2016192. SEM images were taken at the Electron Microscope Facility of Oregon State University. XAS measurements were done at 11-2 at SSRL and 9-BM at the Advanced Photon Source (APS). Argonne National Laboratory. The use of APS at Argonne National Laboratory (ANL) for synchrotron measurements is supported by the Department of Energy under Contract No. DE-AC02-06CH11357. X.L. would like to thank the U.S. Department of Energy (DOE) Office of Electricity (Contract No. 70247A) for their support. Pacific Northwest National Laboratory is a multiprogram laboratory operated by Battelle Memorial Institute for the DOE under Contract DE-AC05-76RL01830.

REFERENCES

(1) Huang, Y. The Discovery of Cathode Materials for Lithium-ion Batteries from the View of Interdisciplinarity. *Interdiscip. Mater.* **2022**, *1*, 323−329.

(2) Piernas Muñoz, M. J., Castillo-Martínez, E. *Prussian Blue Based Batteries SpringerBriefs in Applied Sciences and Technology*; Springer: 2018; Chapter 2, pp. 9−22.

(3) Wu, X.; Shao, M.; Wu, C.; Qian, J.; Cao, Y.; Ai, X.; Yang, H. Low Defect FeFe(CN)6 Framework as Stable Host Material for High Performance Li-Ion Batteries. *ACS Appl. Mater. Interfaces* **2016**, *8*, 23706−23712.

(4) Wu, X.; Xu, Y.; Jiang, H.; Wei, Z.; Hong, J. J.; Hernandez, A. S.; du, F.; Ji, X. NH4+ Topotactic Insertion in Berlin Green: An Exceptionally Long-Cycling Cathode in Aqueous Ammonium-Ion Batteries. *ACS Appl. Energy Mater.* **2018**, *1*, 3077−3083.

(5) Shiga, T.; Kondo, H.; Kato, Y.; Inoue, M. Insertion of Calcium Ion into Prussian Blue Analogue in Nonaqueous Solutions and Its Application to a Rechargeable Battery with Dual Carriers. *J. Phys. Chem. C* **2015**, *119*, 27946−27953.

(6) Qian, J.; Wu, C.; Cao, Y.; Ma, Z.; Huang, Y.; Ai, X.; Yang, H. Prussian Blue Cathode Materials for Sodium-Ion Batteries and Other Ion Batteries. *Adv. Energy Mater.* **2018**, *8*, No. 1702619.

(7) Lim, C. Q. X.; Tan, Z.-K. Prussian White with Near-Maximum Specific Capacity in Sodium-Ion Batteries. *ACS Appl. Energy Mater.* **2021**, *4*, 6214−6220.

(8) Wang, L.; Song, J.; Qiao, R.; Wray, L. A.; Hossain, M. A.; Chuang, Y. D.; Yang, W.; Lu, Y.; Evans, D.; Lee, J. J.; Vail, S.; Zhao, X.; Nishijima, M.; Kakimoto, S.; Goodenough, J. B. Rhombohedral Prussian White as Cathode for Rechargeable Sodium-ion Batteries. *J. Am. Chem. Soc.* **2015**, *137*, 2548−2554.

(9) Tron, A.; Jeong, S.; Park, Y. D.; Mun, J. Aqueous Lithium-Ion Battery of Nano-LiFePO4 with Antifreezing Agent of Ethyleneglycol for Low-Temperature Operation. *ACS Sustainable Chem. Eng.* **2019**, *7*, 14531−14538.

(10) Wessells, C.; Huggins, R. A.; Cui, Y. Recent Results on Aqueous Electrolyte Cells. *J. Power Sources* **2011**, *196*, 2884−2888.

(11) Luo, J. Y.; Cui, W. J.; He, P.; Xia, Y. Y. Raising the Cycling Stability of Aqueous Lithium-ion Batteries by Eliminating Oxygen in the Electrolyte. *Nat. Chem.* **2010**, *2*, 760−765.

(12) Hou, Y.; Wang, X.; Zhu, Y.; Hu, C.; Chang, Z.; Wu, Y.; Holze, R. Macroporous LiFePO4 as a Cathode for an Aqueous Rechargeable Lithium Battery of High Energy Density. *J. Mater. Chem. A* **2013**, *1*, 14713.

(13) Xiao, J. A Granular Approach to Electrode Design. *Science* **2022**, *376*, 455−456.

(14) Yang, D.; Xu, J.; Liao, X. Z.; Wang, H.; He, Y. S.; Ma, Z. F. Prussian Blue without Coordinated Water as a Superior Cathode for Sodium-ion Batteries. *Chem. Commun.* **2015**, *51*, 8181−8184.

(15) He, S.; Zhao, J.; Rong, X.; Xu, C.; Zhang, Q.; Shen, X.; Qi, X.; Li, Y.; Li, X.; Niu, Y.; Li, X.; Han, S.; Gu, L.; Liu, H.; Hu, Y. S. Solvent-free Mechanochemical Synthesis of Na-rich Prussian White Cathodes for High-performance Na-ion Batteries. *Chem. Eng. J.* **2022**, *428*, No. 131083.

(16) Yang, J.; Wang, H.; Lu, L.; Shi, W.; Zhang, H. Large-Scale Synthesis of Berlin Green Fe[Fe(CN)6] Microcubic Crystals. *Cryst. Growth Des.* **2006**, *6*, 2438−2440.

(17) Wang, W.; Gang, Y.; Hu, Z.; Yan, Z.; Li, W.; Li, Y.; Gu, Q. F.; Wang, Z.; Chou, S. L.; Liu, H. K.; Dou, S. X. Reversible Structural Evolution of Sodium-Rich Rhombohedral Prussian Blue for Sodium-ion Batteries. *Nat. Commun.* **2020**, *11*, 980.

(18) Ghosh, S. N. Infrared Spectra of the Prussian Blue Analogs. *J. Inorg. Nucl. Chem.* **1974**, *36*, 2465−2466.

(19) Shen, L.; Jiang, Y.; Liu, Y.; Ma, J.; Sun, T.; Zhu, N. High-stability Monoclinic Nickel Hexacyanoferrate Cathode Materials for Ultrafast Aqueous Sodium ion Battery. *Chem. Eng. J.* **2020**, *388*, No. 124228.

(20) Wang, B.; Wang, X.; Liang, C.; Yan, M.; Jiang, Y. An All-Prussian-Blue-Based Aqueous Sodium-Ion Battery. *ChemElectroChem* **2019**, *6*, 4848−4853.

(21) Piernas-Muñoz, M. J.; Castillo-Martínez, E.; Bondarchuk, O.; Armand, M.; Rojo, T. Higher Voltage Plateau Cubic Prussian White for Na-ion Batteries. *J. Power Sources* **2016**, *324*, 766−773.
(22) Yamashita, T.; Hayes, P. Analysis of XPS Spectra of Fe2+ and Fe3+ Ions in Oxide Materials. *Appl. Surf. Sci.* **2008**, *254*, 2441−2449.
(23) Zhou, P.; Xue, D.; Luo, H.; Chen, X. Fabrication, Structure, and Magnetic Properties of Highly Ordered Prussian Blue Nanowire Arrays. *Nano Lett.* **2002**, *2*, 845−847.
(24) Huang, Q.; Yang, J.; Ng, C. B.; Jia, C.; Wang, Q. A Redox Flow Lithium Battery Based on the Redox Targeting Reactions Between LiFePO4 and Iodide. *Energy Environ. Sci.* **2016**, *9*, 917−921.
(25) Triwibowo, J.; Priyono, S.; Purawiardi, I.; Lestariningsih, T.; Ratri, C. R. Study on Electrochemical Performance of Carbon-coated LiFePO4 as Cathode Material for Lithium-ion Batteries. *AIP Conf. Proc.* **2016**, *1755*, 150009.
(26) Qiu, S.; Lucero, M.; Wu, X.; Wang, Q.; Wang, M.; Wang, Y.; Samarakoon, W. S.; Bolding, M. R.; Yang, Z.; Huang, Y.; Xu, Z. J. Revealing the Fast and Durable Na+ Insertion Reactions in a Layered Na3Fe3(PO4)4 Anode for Aqueous Na-Ion Batteries. *ACS Mater. Au* **2022**, *2*, 63−71.
(27) Qiu, S.; Wu, X.; Wang, M.; Lucero, M.; Wang, Y.; Wang, J.; Yang, Z.; Xu, W.; Wang, Q.; Gu, M.; Wen, J.; Huang, Y.; Xu, Z. J.; Feng, Z. NASICON-type Na3Fe2(PO4)3 as a Low-cost and High-rate Anode Material for Aqueous Sodium-ion Batteries. *Nano Energy* **2019**, *64*, No. 103941.
(28) Chen, C.; Wen, Y.; Hu, X.; Ji, X.; Yan, M.; Mai, L.; Hu, P.; Shan, B.; Huang, Y. Na(+) Intercalation Pseudocapacitance in Graphene-coupled Titanium Oxide Enabling Ultra-fast Sodium Storage and Long-term Cycling. *Nat. Commun.* **2015**, *6*, 6929.
(29) Gogotsi, Y.; Penner, R. M. Energy Storage in Nanomaterials - Capacitive, Pseudocapacitive, or Battery-like? *ACS Nano* **2018**, *12*, 2081−2083.
(30) Fleischmann, S.; Mitchell, J. B.; Wang, R.; Zhan, C.; Jiang, D. E.; Presser, V.; Augustyn, V. Pseudocapacitance: From Fundamental Understanding to High Power Energy Storage Materials. *Chem. Rev.* **2020**, *120*, 6738−6782.
(31) Dau, H.; Liebisch, P.; Haumann, M. X-ray Absorption Spectroscopy to Analyze Nuclear Geometry and Electronic Structure of Biological Metal Centers–Potential and Questions Examined with Special Focus on the Tetra-nuclear Manganese Complex of Oxygenic Photosynthesis. *Anal. Bioanal. Chem.* **2003**, *376*, 562−583.
(32) Lucero, M.; Qiu, S.; Feng, Z. In-situ Characterizations of Solid−solid Interfaces in Solid-state Batteries using Synchrotron X-ray Techniques. *Carbon Energy* **2021**, *3*, 762−783.
(33) Wang, M.; Arnadottir, L.; Xu, Z. J.; Feng, Z. In Situ X-ray Absorption Spectroscopy Studies of Nanoscale Electrocatalysts. *Nanomicro Lett.* **2019**, *11*, 47.
(34) Wang, M.; Feng, Z. Pitfalls in X-ray Absorption Spectroscopy Analysis and Interpretation: A Practical Guide for General Users. *Curr. Opin. Electrochem.* **2021**, *30*, No. 100803.
(35) Sandstrom, S. K.; Jiang, H.; Lucero, M.; Xu, Y.; Gallagher, T. C.; Cao, M.; Feng, Z.; Ji, X. Reversible Electrochemical Conversion from Selenium to Cuprous Selenide. *Chem. Commun.* **2021**, *57*, 10703−10706.
(36) You, Y.; Yu, X.; Yin, Y.; Nam, K.-W.; Guo, Y.-G. Sodium Iron Hexacyanoferrate with High Na Content as a Na-rich Cathode Material for Na-ion Batteries. *Nano Res.* **2015**, *8*, 117−128.
(37) Lee, M. H.; Kim, S. J.; Chang, D.; Kim, J.; Moon, S.; Oh, K.; Park, K. Y.; Seong, W. M.; Park, H.; Kwon, G.; Lee, B.; Kang, K. Toward a Low-cost High-voltage Sodium Aqueous Rechargeable Battery. *Mater. Today* **2019**, *29*, 26−36.
(38) Xie, B.; Zuo, P.; Wang, L.; Wang, J.; Huo, H.; He, M.; Shu, J.; Li, H.; Lou, S.; Yin, G. Achieving Long-life Prussian Blue Analogue Cathode for Na-ion Batteries via Triple-cation Lattice Substitution and Coordinated Water Capture. *Nano Energy* **2019**, *61*, 201−210.
(39) Wei, C.; Feng, Z.; Baisariyev, M.; Yu, L.; Zeng, L.; Wu, T.; Zhao, H.; Huang, Y.; Bedzyk, M. J.; Sritharan, T.; Xu, Z. J. Valence Change Ability and Geometrical Occupation of Substitution Cations Determine the Pseudocapacitance of Spinel Ferrite XFe2O4 (X = Mn, Co, Ni, Fe). *Chem. Mater.* **2016**, *28*, 4129−4133.
(40) Samain, L.; Grandjean, F.; Long, G. J.; Martinetto, P.; Bordet, P.; Strivay, D. Relationship between the Synthesis of Prussian Blue Pigments, Their Color, Physical Properties, and Their Behavior in Paint Layers. *J. Phys. Chem. C* **2013**, *117*, 9693−9712.

https://doi.org/10.1021/acsami.3c07304
ACS Appl. Mater. Interfaces 2023, 15, 36366−36372